Comparing real-time coupled-cluster methods through simulation of collective Rabi oscillations

Andreas S. Skeidsvoll

Department of Chemistry, Norwegian University of Science and Technology, 7491 Trondheim, Norway

Henrik Koch *

Scuola Normale Superiore, Piazza dei Cavalieri 7, 56126 Pisa, Italy
and Department of Chemistry, Norwegian University of Science and Technology, 7491 Trondheim, Norway

The time-dependent equation-of-motion coupled-cluster singles and doubles (TD-EOM-CCSD) and time-dependent coupled-cluster singles and doubles (TDCCSD) methods are compared by simulating Rabi oscillations for distant atoms in a classical electromagnetic field. While the TD-EOM-CCSD simulations are numerically stable, the oscillating time-dependent energy expectation value displays an incorrect scaling with the number of atoms resonant with the field. On the other hand, the TDCCSD simulations exhibit the correct scaling in the initial stages of the Rabi cycle but break down when the multiatom system approaches complete population inversion. The numerical stability of the TDCCSD simulations is shown to be very sensitive to any interactions between the atoms and to left amplitudes that do not participate in the expression for time-dependent expectation values for noninteracting atoms. Moreover, we introduce a general theoretical framework for describing the two methods, where the cluster amplitude time derivatives serve as auxiliary conditions related to a shift of the time-dependent Hamiltonian matrix. In this framework, time-dependent coupled-cluster methods exhibit a shifted Hamiltonian matrix with a block upper triangular structure in terms of the number of excited noninteracting subsystems, explaining the correct scaling properties of the TDCCSD method.

I. INTRODUCTION

With recent developments in the shaping and amplification of laser pulses, the production of short and strong pulses can now be realized in several frequency domains [1–3]. The progress has sparked further interest in the dynamical and nonlinear response of molecules to strong fields, which can involve a high number of quantum states [4], since many of the states that are inaccessible by a single-photon transition, either energetically or by symmetry selection rules, can be accessed by a multiphoton transition [5,6].

The ultrafast nonlinear response of molecules to strong fields can give an extended degree of dynamic control of chemical reactions [7–9]. It can also reveal information about the system that is inaccessible in weaker fields, which can be used for improving the imaging of different reaction stages [5,8]. Nevertheless, the involved coupling between the numerous affected states can lead to an intricate relationship between the shape and strength of laser pulses and the molecular response, which calls for the interpretation by appropriate quantum chemistry methods [10].

Both the accuracy and computational complexity of quantum chemistry methods often increase with the order of approximation of the particle correlations in the system [10,11] and the size of the finite basis set [12], but the accuracy also depends heavily on the mathematical structure of the method. Considerable effort is spent on constructing optimal methods for a given order of computational complexity, with respect to both numerical stability and correspondence to experimental results for various systems. Real-time variants of quantum chemistry methods are convenient for modeling multiphoton transitions in systems [13], as expressions for the high-order frequency response can be difficult to both derive and solve numerically.

The well-established single-reference coupled-cluster (CC) hierarchy of methods often gives accurate and rapidly converging molecular properties [14] for states with weak multireference character [15]. An important reason for this accuracy is the physically reasonable scaling properties of the methods, even when the cluster operator is truncated. For instance, the energy of the ground state is size extensive, meaning it scales linearly with the number of noninteracting identical subsystems [16]. In the equation-of-motion (EOM)–CC framework, the excitation energies are size intensive, meaning they do not scale with the number of noninteracting subsystems [17]. In the linear-response framework, which is based on time-dependent coupled-cluster theory, ground-state–excited-state transition moments are also size intensive [18]. Truncated configuration-interaction methods, on the other hand, do not possess these properties and errors generally increase with the size of the simulated system [19].

Traditionally, coupled-cluster methods have almost exclusively been treated in the frequency domain, but the past decade has witnessed an increased exploration into their

*henrik.koch@sns.it

real-time behavior [13]. As demonstrated by Pedersen and Kvaal [20] and further investigated by Kristiansen *et al.* [21], the exponential parametrization makes the standard time-dependent coupled-cluster (TDCC) method inherently unstable whenever the reference determinant weight is depleted by a strong field. These instabilities can require the use of exceedingly small time steps in numerical solutions and can at times also lead to breakdowns that cannot be solved by decreasing the time-step size.

The orbital adaptive time-dependent coupled-cluster method, which requires the solution of an additional set of linear equations at each time step, has been shown to be more stable than TDCC. Nonetheless, the method can still fail at higher field strengths, where the reference determinant weight can become greater than one [21].

Variants of the TD-EOM-CC method have also been used for modeling laser-molecule interactions, but only a handful of applications have included the full nonlinear real-time propagation of the laser-driven electron dynamics [13,22–24]. In these cases, the TD-EOM-CC equations were expressed in the basis obtained by diagonalizing the field-free equation-of-motion coupled-cluster Hamiltonian. We instead express the equations in the elementary basis, leading to equations that are simple to implement and have computational and memory requirements that scale more favorably with respect to system size than the full diagonal basis equations. This makes the formulation particularly useful for assessing the short-time and nonlinear behavior of the TD-EOM-CC method.

The paper is organized as follows. In Sec. II the TD-EOM-CC and TDCC methods are described in a general theoretical framework and it is shown how the time derivative of the cluster amplitudes affects the analytical scaling properties of the truncated variants of the methods. Section III outlines the computational methods used to simulate distant atoms undergoing semiclassical Rabi oscillations in a resonant electromagnetic field. In Sec. IV the results of the simulations are presented and discussed, including a demonstration of how the time-dependent energy expectation value scales with respect to system size in the TD-EOM-CCSD and TDCCSD methods. The key findings are summarized in Sec. V.

II. THEORY

A. System

The time-dependent system of the molecule and the electromagnetic field is described by the Hamiltonian

$$H(t) = H^{(0)} + V(t). \tag{1}$$

The field-free molecular system is described by the Hamiltonian $H^{(0)}$ and the interaction between the molecular system and the electromagnetic field is described by $V(t)$. We describe the interaction semiclassically, in the dipole approximation and length gauge. This gives $V(t) = -\boldsymbol{\mu} \cdot \boldsymbol{\mathcal{E}}(t)$, where $\boldsymbol{\mu}$ is the electric dipole moment vector and $\boldsymbol{\mathcal{E}}(t)$ the classical time-dependent electric-field vector. The system is also treated within the Born-Oppenheimer approximation, with fixed nuclei.

B. Time dependence in coupled-cluster methods

The TD-EOM-CC and TDCC methods can be written in a general theoretical framework by expressing the time-dependent ket and bra vectors as

$$|\Psi(t)\rangle = e^{T(t)} R(t) |\mathrm{HF}\rangle e^{i\epsilon(t)}, \tag{2}$$

$$\langle\tilde{\Psi}(t)| = e^{-i\epsilon(t)} \langle\mathrm{HF}| L(t) e^{-T(t)}, \tag{3}$$

where the cluster operator

$$T(t) = \sum_{\mu>0} \tau_\mu t_\mu(t) \tag{4}$$

and the right and left operators

$$R(t) = \sum_{\kappa\geqslant 0} \tau_\kappa r_\kappa(t), \quad L(t) = \sum_{\kappa\geqslant 0} l_\kappa(t) \tilde{\tau}_\kappa^\dagger. \tag{5}$$

The function $\epsilon(t)$ represents a time-dependent global phase, which does not enter into expressions for physical observables but can impact the performance of numerical implementations. The elementary operators τ_0 and $\tilde{\tau}_0^\dagger$ are the unit operator

$$\tau_0 = \tilde{\tau}_0^\dagger = \mathbb{1} \tag{6}$$

and the elementary operators τ_μ and $\tilde{\tau}_\mu^\dagger$, where $\mu > 0$, excite and deexcite electrons between occupied and virtual Hartree-Fock molecular orbitals, respectively,

$$\tau_\mu|\mathrm{HF}\rangle = |\mu\rangle, \quad \langle\mathrm{HF}|\tilde{\tau}_\mu^\dagger = \langle\tilde{\mu}|, \tag{7}$$

$$\tilde{\tau}_\mu^\dagger|\mathrm{HF}\rangle = 0, \quad \langle\mathrm{HF}|\tau_\mu = 0. \tag{8}$$

These operators are chosen so that the resulting elementary kets and bras are biorthonormal,

$$\langle\tilde{\kappa}|\lambda\rangle = \delta_{\kappa\lambda}, \quad \kappa \geqslant 0, \ \lambda \geqslant 0, \tag{9}$$

where $\delta_{\kappa\lambda}$ is the Kronecker delta. The sums over excitation levels in Eqs. (4) and (5) can be truncated in order to reduce computational scaling, yielding the coupled-cluster singles method when only single excitations are included, coupled-cluster singles and doubles (CCSD) when both single and double excitations are included, and so on.

The equations for the time dependence of the parameters of Eq. (5) can be derived from the right and left time-dependent Schrödinger equations (TDSEs)

$$i\frac{d}{dt}|\Psi(t)\rangle = H(t)|\Psi(t)\rangle, \tag{10}$$

$$-i\frac{d}{dt}\langle\tilde{\Psi}(t)| = \langle\tilde{\Psi}(t)|H(t). \tag{11}$$

Inserting Eq. (2) into Eq. (10) before projecting onto $e^{-i\epsilon(t)}\langle\tilde{\kappa}|e^{-T(t)}$ and likewise inserting Eq. (3) into Eq. (11) before projecting onto $e^{T(t)}|\lambda\rangle e^{i\epsilon(t)}$, the elementary-basis matrix-vector TDSEs are obtained as

$$i\frac{dr_\kappa(t)}{dt} = \sum_{\lambda\geqslant 0} \tilde{H}_{\kappa\lambda}(t) r_\lambda(t), \tag{12}$$

$$-i\frac{dl_\lambda(t)}{dt} = \sum_{\kappa\geqslant 0} l_\kappa(t) \tilde{H}_{\kappa\lambda}(t), \tag{13}$$

where the shifted Hamiltonian

$$\tilde{H}(t) = H(t) + \frac{d\epsilon(t)}{dt} - i\frac{dT(t)}{dt}. \tag{14}$$

The elements of the elementary-basis coupled-cluster matrix $\mathbf{O}(t)$ of operator $O(t)$ are given by

$$O_{\kappa\lambda}(t) = \langle\tilde{\kappa}|\bar{O}(t)|\lambda\rangle, \tag{15}$$

where an overbar is used to denote the similarity transformation by the exponentiated time-dependent cluster operator,

$$\bar{O}(t) = e^{-T(t)}O(t)e^{T(t)}. \tag{16}$$

By invoking the resolution of identity $\mathbb{1} = |\mathrm{HF}\rangle\langle\mathrm{HF}| + \sum_{\mu>0}|\mu\rangle\langle\tilde{\mu}|$, the matrix elements of the shifted Hamiltonian in Eq. (14) can be expressed as

$$\begin{aligned}\tilde{H}_{\kappa\lambda}(t) &= \langle\tilde{\kappa}|\bar{H}(t)|\lambda\rangle \\ &\quad + \langle\tilde{\kappa}|\left(\frac{d\epsilon(t)}{dt} - i\sum_{\mu>0}\tau_\mu\frac{dt_\mu(t)}{dt}\right)|\lambda\rangle \\ &= \langle\tilde{\kappa}|[\bar{H}(t),\tau_\lambda]|\mathrm{HF}\rangle \\ &\quad + \langle\tilde{\kappa}|\tau_\lambda\left(|\mathrm{HF}\rangle\langle\mathrm{HF}| + \sum_{\mu>0}|\mu\rangle\langle\tilde{\mu}|\right)\bar{H}(t)|\mathrm{HF}\rangle \\ &\quad + \langle\tilde{\kappa}|\left(\frac{d\epsilon(t)}{dt} - i\sum_{\mu>0}\tau_\mu\frac{dt_\mu(t)}{dt}\right)|\lambda\rangle \\ &= U_{\kappa\lambda}(t) + \tilde{D}_{\kappa\lambda}(t) + \tilde{L}_{\kappa\lambda}(t), \end{aligned} \tag{17}$$

where

$$U_{\kappa\lambda}(t) = \langle\tilde{\kappa}|[\bar{H}(t),\tau_\lambda]|\mathrm{HF}\rangle, \tag{18}$$

$$\tilde{D}_{\kappa\lambda}(t) = \delta_{\kappa\lambda}\left(\langle\mathrm{HF}|\bar{H}(t)|\mathrm{HF}\rangle + \frac{d\epsilon(t)}{dt}\right), \tag{19}$$

$$\tilde{L}_{\kappa\lambda}(t) = \sum_{\mu>0}\langle\tilde{\kappa}|\tau_\mu|\lambda\rangle\left(\langle\tilde{\mu}|\bar{H}(t)|\mathrm{HF}\rangle - i\frac{dt_\mu(t)}{dt}\right). \tag{20}$$

To explain the choices of the names of the three terms in Eq. (17) in anticipation of the discussion in Sec. II C, we remark that the commutator $[\bar{H}(t),\tau_\lambda]$ in Eq. (18) implies that the $\mathbf{U}(t)$ term of the shifted Hamiltonian matrix for two noninteracting subsystems is block upper triangular in terms of the number of excited subsystems. Furthermore, the excitation operator τ_μ in Eq. (20) implies that the $\mathbf{L}(t)$ term is block lower triangular, and the Kronecker delta $\delta_{\kappa\lambda}$ in Eq. (19) implies that the $\mathbf{D}(t)$ term is (block) diagonal. Once all time-dependent amplitudes have been found at a given point in time t, the time-dependent expectation values of the time-dependent operator $O(t)$ can be obtained through

$$\begin{aligned}\langle O(t)\rangle &= \langle\tilde{\Psi}(t)|O(t)|\Psi(t)\rangle = \sum_{\kappa,\lambda\geqslant 0} l_\kappa(t)O_{\kappa\lambda}(t)r_\lambda(t) \\ &= \boldsymbol{l}^T(t)\boldsymbol{O}(t)\boldsymbol{r}(t). \end{aligned} \tag{21}$$

The indeterminate matrix-vector equations in Eqs. (12) and (13) give a unified representation of the TD-EOM-CC and TDCC methods, since the two methods can be recovered by imposing constraints on the cluster amplitude time derivatives and assuming that the propagation starts from the time-independent field-free ground state. This state can be defined by the operators $T^{(0)}$, $R_0^{(0)}$, and $L_0^{(0)}$ by setting the right and left amplitudes $r_{\mu 0}^{(0)} = 0$ and $r_{00}^{(0)} = l_{00}^{(0)} = 1$ and letting the ground-state

cluster amplitudes $t_\mu^{(0)}$ and left amplitudes $l_{0\mu}^{(0)}$ be determined as solutions of the field-free ground-state equations

$$\langle\tilde{\mu}|e^{-T^{(0)}}H^{(0)}e^{T^{(0)}}|\mathrm{HF}\rangle = 0, \tag{22}$$

$$\left(\langle\mathrm{HF}| + \sum_{\mu>0}l_{0\mu}^{(0)}\langle\tilde{\mu}|\right)[e^{-T^{(0)}}H^{(0)}e^{T^{(0)}},\tau_\nu]|\mathrm{HF}\rangle = 0. \tag{23}$$

Thus, the ground state is defined, with an inherent ambiguity related to the time-dependent global phase.

The TD-EOM-CC method is usually derived without the time-dependent phase factor and without consideration for the time dependence of the cluster amplitudes [22–24]. However, the cluster amplitude time dependence can equivalently be removed after the derivation of Eqs. (12) and (13) by setting

$$i\frac{dt_\mu(t)}{dt} = 0. \tag{24}$$

Since we also assume that the propagation starts from the ground state, Eq. (24) implies that $T(t) = T^{(0)}$, and Eq. (17) can thus be expressed as

$$\tilde{H}_{\kappa\lambda}(t) = U_{\kappa\lambda}(t) + \tilde{D}_{\kappa\lambda}(t) + \tilde{L}_{\kappa\lambda}(t), \tag{25}$$

where

$$U_{\kappa\lambda}(t) = \langle\tilde{\kappa}|[e^{-T^{(0)}}H(t)e^{T^{(0)}},\tau_\lambda]|\mathrm{HF}\rangle, \tag{26}$$

$$\tilde{D}_{\kappa\lambda}(t) = \delta_{\kappa\lambda}\left(\langle\mathrm{HF}|e^{-T^{(0)}}H(t)e^{T^{(0)}}|\mathrm{HF}\rangle + \frac{d\epsilon(t)}{dt}\right), \tag{27}$$

$$\tilde{L}_{\kappa\lambda}(t) = \sum_{\mu>0}\langle\tilde{\kappa}|\tau_\mu|\lambda\rangle\langle\tilde{\mu}|e^{-T^{(0)}}V(t)e^{T^{(0)}}|\mathrm{HF}\rangle, \tag{28}$$

and the $H^{(0)}$ term of $\tilde{L}_{\kappa\lambda}(t)$ is zero because of Eq. (22).

In the TDCC method, the time derivatives of the cluster amplitudes are given by [25]

$$i\frac{dt_\mu(t)}{dt} = \langle\tilde{\mu}|\bar{H}(t)|\mathrm{HF}\rangle. \tag{29}$$

From this expression, Eq. (20) can be seen to reduce to

$$\tilde{L}_{\kappa\lambda}(t) = 0, \tag{30}$$

implying that

$$\tilde{H}_{\kappa\lambda}(t) = U_{\kappa\lambda}(t) + \tilde{D}_{\kappa\lambda}(t), \tag{31}$$

where $U_{\kappa\lambda}(t)$ and $\tilde{D}_{\kappa\lambda}(t)$ are given by Eqs. (18) and (19), respectively. In Ref. [25] the time derivative of the phase is furthermore constrained by

$$\frac{d\epsilon(t)}{dt} = -\langle\mathrm{HF}|\bar{H}(t)|\mathrm{HF}\rangle, \tag{32}$$

which leads to $\tilde{D}_{\kappa\lambda}(t) = 0$. Nonetheless, other constraints lead to equivalent formulations of the TDCC method, owing to the flexibility with respect to the time-dependent global phase.

The ket and bra vectors used in standard derivations of the TDCC method [25] do not include the right operator $R(t)$ in Eq. (2) nor the time dependence of the reference component of $L(t)$ in Eq. (3). To demonstrate that the TDCC method is still retrieved when the propagation starts from the ground state, we start by noting that Eqs. (12), (31), and (32) imply that the time derivatives of all $r_\kappa(t)$ are zero whenever all

$r_\mu(t)$ are zero for $\mu > 0$. Furthermore, Eqs. (13), (31), and (32) imply that the time derivative of $l_0(t)$ is zero. Therefore, when the propagation starts from the coupled-cluster ground state, $r_\mu(t) = 0$ and $l_0(t) = r_0(t) = 1$ at all times t. For $\kappa > 0$, Eq. (13) is hence equivalent to the expression for the left amplitude time derivatives in Ref. [25], and the TDCC method is retrieved despite the additional flexibility in the parametrization of Eqs. (2) and (3).

The choice of cluster amplitude time derivatives has major implications for the properties of the resulting method. In the TD-EOM-CC method, Eq. (24) implies that the cluster amplitudes do not change with time, and real arithmetic can be used to reduce the cost of TD-EOM-CC propagation provided the cluster amplitudes of the ground state are real. In the TDCC method, on the one hand, Eq. (29) implies that the time-dependent cluster amplitudes are complex, requiring the use of complex arithmetic. The TDCC time derivatives also imply that Eqs. (12) and (13) are nonlinear in the time-dependent parameters, and the expression and interpretation of the time-dependent state in terms of EOM-CC states is thus nontrivial [26]. For the TD-EOM-CC method, on the other hand, Eqs. (12) and (13) are linear in the time-dependent parameters, and the time independence of the cluster operator allows the method to be expressed in the basis of the field-free EOM-CC states. This can be shown by operating with the resolution of identity

$$\mathbb{1} = \sum_{i \geqslant 0} \big|\psi_i^{(0)}\big\rangle\big\langle\tilde{\psi}_i^{(0)}\big| \tag{33}$$

on both Eqs. (2) and (3), where the ket and bra of the field-free EOM-CC state i can be expressed as

$$\big|\psi_i^{(0)}\big\rangle = R_i^{(0)} e^{T^{(0)}} |\text{HF}\rangle, \quad \big\langle\tilde{\psi}_i^{(0)}\big| = \langle\text{HF}| e^{-T^{(0)}} L_i^{(0)} \tag{34}$$

and the amplitudes of the operators $R_i^{(0)} = \sum_{\kappa \geqslant 0} \tau_\kappa R_{\kappa i}^{(0)}$ and $L_i^{(0)} = \sum_{\kappa \geqslant 0} L_{i\kappa}^{(0)} \tilde{\tau}_\kappa^\dagger$ are the right and left eigenvectors of the field-free coupled-cluster Hamiltonian matrix $H_{\kappa\lambda}^{(0)} = \langle\tilde{\kappa}| e^{-T^{(0)}} H^{(0)} e^{T^{(0)}} |\lambda\rangle$. By letting $\langle\tilde{\psi}_i^{(0)}|\Psi(t)\rangle = s_i(t)$ and $\langle\tilde{\Psi}(t)|\psi_i^{(0)}\rangle = k_i(t)$, the elementary basis formulation of the TD-EOM-CC method presented here can be seen to be equivalent to the diagonal basis formulation of Ref. [24], up to the factor containing the time-dependent global phase. As demonstrated in that reference, field-free EOM-CC states that do not participate in the dynamics can be removed from the diagonal basis in order to reduce computational costs. However, the full elementary basis formulation of the TD-EOM-CC method, as given by Eqs. (12), (13), and (25), straightforwardly ensures the inclusion of all transitions without requiring the calculation of all field-free EOM-CC states and transition moments.

C. Scaling properties of real-time coupled-cluster methods

In order to investigate theoretically the scaling properties of methods based on the parametrization in Eqs. (2) and (3), we assume that the system is composed of multiple noninteracting subsystems. We let τ_{λ_I} denote an elementary excitation operator and $\tilde{\tau}_{\kappa_I}^\dagger$ an elementary deexcitation operator of subsystem I. The elementary excitation and deexcitation operators of the composite system can be constructed as

tensor products of corresponding operators of the different subsystems. Untruncated TD-EOM-CC and TDCC methods can represent all these tensor products, since the excitation and deexcitation levels of the methods are not limited. In truncated methods, however, all elementary excitation and deexcitation operators that exceed the truncation level specific to the method are excluded, which can lead to errors related to the scaling from one to multiple subsystems.

For two subsystems $I \in \{A, B\}$, the elementary excitation and deexcitation operators of the composite system can be constructed as the tensor products $\tau_{\lambda_A} \otimes \tau_{\lambda_B}$ and $\tilde{\tau}_{\kappa_A}^\dagger \otimes \tilde{\tau}_{\kappa_B}^\dagger$. We split the sets of these operators into four partitions, which we label 0, A, B, and AB. The 0 partition includes the operators that do not change the excitation level of the subsystems, $\tau_{0_A} \otimes \tau_{0_B}$ and $\tilde{\tau}_{0_A}^\dagger \otimes \tilde{\tau}_{0_B}^\dagger$. The A partition includes the operators that change the excitation level of subsystem A only, $\tau_{\mu_A} \otimes \tau_{0_B}$ and $\tilde{\tau}_{\mu_A}^\dagger \otimes \tilde{\tau}_{0_B}^\dagger$, and the B partition the operators that change the excitation level of subsystem B only, $\tau_{0_A} \otimes \tau_{\mu_B}$ and $\tilde{\tau}_{0_A}^\dagger \otimes \tilde{\tau}_{\mu_B}^\dagger$, where $\mu > 0$. The AB partition includes the operators that change the excitation level of both subsystems, $\tau_{\nu_A} \otimes \tau_{\nu_B}$ and $\tilde{\tau}_{\mu_A}^\dagger \otimes \tilde{\tau}_{\mu_B}^\dagger$, where $\mu > 0$ and $\nu > 0$. Truncation can affect the AB partition, since the tensor products of the truncated subsystem operators can include excitations and deexcitations that in combination go beyond the truncation level of the method. In the following, we assess the general impact of this truncation on the TD-EOM-CC and TDCC methods, without limiting the discussion to any particular truncation level.

We start by assuming that the cluster amplitudes corresponding to the operators $\tau_{\mu_A} \otimes \tau_{\mu_B}$ are zero at a given time t. The cluster operator $T(t)$ can then be written as the tensor sum

$$T(t) = T_A(t) \otimes I_B + I_A \otimes T_B(t), \tag{35}$$

where $T_I(t)$ is the cluster operator for subsystem I. Since operators on noninteracting subsystems commute, we have that

$$e^{\pm[T_A(t) \otimes I_B + I_A \otimes T_B(t)]} = e^{\pm T_A(t)} \otimes e^{\pm T_B(t)}. \tag{36}$$

We furthermore let $O(t)$ be any operator that does not involve any interaction between the two subsystems and thus can be written as the tensor sum

$$O(t) = O_A(t) \otimes I_B + I_A \otimes O_B(t), \tag{37}$$

where $O_A(t)$ and $O_B(t)$ are subsystem operators. Equation (36) then implies that the similarity transformed operator in Eq. (16) can be written as the tensor sum

$$\bar{O}(t) = e^{-T_A(t)} O_A(t) e^{T_A(t)} \otimes I_B + I_A \otimes e^{-T_B(t)} O_B(t) e^{T_B(t)}$$
$$= \bar{O}_A(t) \otimes I_B + I_A \otimes \bar{O}_B(t), \tag{38}$$

which does not contain terms where both subsystems are excited simultaneously.

We furthermore assume that the time-dependent Hamiltonian $H(t)$ does not involve any interaction between the two subsystems, implying that it can be written in the form of Eq. (37). In the TDCC method, the time derivative of the cluster amplitudes in Eq. (29) can, for the AB partition, then

be written as

$$i\frac{dt_{\mu_A\mu_B}(t)}{dt} = (\langle\tilde{\mu}_A|\otimes\langle\tilde{\mu}_B|)[\bar{H}_A(t)\otimes I_B + I_A\otimes\bar{H}_B(t)]$$
$$\times (|HF_A\rangle\otimes|HF_B\rangle) = 0. \quad (39)$$

If Eq. (35) is true at the initial time, it will therefore remain true for later times in the TDCC method provided the Hamiltonian still separates as $H_A(t)\otimes I_B + I_A\otimes H_B(t)$. In the TD-EOM-CC method, the time derivatives of the AB partition cluster amplitudes are also zero, as seen by Eq. (24).

We use the subscript $\parallel$ to denote that all amplitudes and matrix elements corresponding to the excitation and deexcitation operators that are not represented in truncated methods have been set to zero. This is used to formulate the truncated methods in the untruncated product basis, for a more straightforward comparison to untruncated methods. Accordingly, the truncated right and transposed left amplitude vectors $\mathbf{r}_\parallel$ and $\mathbf{l}_\parallel^T$ are obtained by eliminating components from the untruncated $\mathbf{r}$ and $\mathbf{l}^T$ and can, in the partitioned product bases, be written as

$$\mathbf{r}_\parallel = \begin{pmatrix} r_0 \\ \mathbf{r}_A \\ \mathbf{r}_B \\ (\mathbf{r}_{AB})_\parallel \end{pmatrix}, \quad \mathbf{l}_\parallel^T = (l_0 \quad \mathbf{l}_A \quad \mathbf{l}_B \quad (\mathbf{l}_{AB})_\parallel), \quad (40)$$

where only the AB partitions are affected by the truncation. Moreover, the truncated operator matrix $\mathbf{O}_\parallel$ is obtained from $\mathbf{O}$, which is the projection of Eq. (38) onto the kets $\tau_{\lambda_A}|HF_A\rangle\otimes\tau_{\lambda_B}|HF_B\rangle$ and bras $\langle HF_A|\tilde{\tau}_{\kappa_A}^\dagger\otimes\langle HF_B|\tilde{\tau}_{\kappa_B}^\dagger$. In the partitioned product bases, this matrix can be written as

$$\mathbf{O}_\parallel = \begin{pmatrix} O_{00} & \mathbf{O}_{0A} & \mathbf{O}_{0B} & \mathbf{0} \\ \mathbf{O}_{A0} & \mathbf{O}_{AA} & \mathbf{0} & (\mathbf{O}_{AAB})_\parallel \\ \mathbf{O}_{B0} & \mathbf{0} & \mathbf{O}_{BB} & (\mathbf{O}_{BAB})_\parallel \\ \mathbf{0} & (\mathbf{O}_{ABA})_\parallel & (\mathbf{O}_{ABB})_\parallel & (\mathbf{O}_{ABAB})_\parallel \end{pmatrix}, \quad (41)$$

where only the AB partition row and column are affected by the truncation.

We proceed to investigate whether time-dependent expectation values in truncated methods, given by

$$\langle O(t)\rangle_\parallel = \mathbf{l}_\parallel^T(t)\mathbf{O}_\parallel(t)\mathbf{r}_\parallel(t), \quad (42)$$

have any dependence on the truncated AB partition, as this would imply that the general scaling properties of the method are incorrect. Assuming that the state of the system is known at $t = t_0$, the time-dependent right and transposed left amplitude vectors of truncated methods can be given as exact solutions of the truncated right and left matrix TDSEs (12) and (13),

$$\mathbf{r}_\parallel(t) = \mathbf{U}_\parallel(t, t_0)\mathbf{r}_\parallel(t_0), \quad \mathbf{l}_\parallel^T(t) = \mathbf{l}_\parallel^T(t_0)\mathbf{U}_\parallel(t_0, t), \quad (43)$$

where

$$\mathbf{U}_\parallel(t, t_0) = \mathbf{I}_\parallel + \sum_{n=0}^\infty (-i)^n \int_{t_0}^t dt_1 \int_{t_0}^{t_1} dt_2$$
$$\cdots \int_{t_0}^{t_{n-1}} dt_n \tilde{\mathbf{H}}_\parallel(t_1)\cdots\tilde{\mathbf{H}}_\parallel(t_n) \quad (44)$$

and $\mathbf{I}$ is the identity matrix. Inserting Eq. (43) into Eq. (42), we get that

$$\langle O(t)\rangle_\parallel = \mathbf{l}_\parallel^T(t_0)\mathbf{U}_\parallel(t_0, t)\mathbf{O}_\parallel(t)\mathbf{U}_\parallel(t, t_0)\mathbf{r}_\parallel(t_0). \quad (45)$$

In general, the truncated shifted Hamiltonian matrices taking part in this equation have the same block structure as Eq. (41), namely,

$$\tilde{\mathbf{H}}_\parallel(t)$$
$$= \begin{pmatrix} \tilde{\mathbf{H}}_{00}(t) & \tilde{\mathbf{H}}_{0A}(t) & \tilde{\mathbf{H}}_{0B}(t) & \mathbf{0} \\ \tilde{\mathbf{H}}_{A0}(t) & \tilde{\mathbf{H}}_{AA}(t) & \mathbf{0} & [\tilde{\mathbf{H}}_{AAB}(t)]_\parallel \\ \tilde{\mathbf{H}}_{B0}(t) & \mathbf{0} & \tilde{\mathbf{H}}_{BB}(t) & [\tilde{\mathbf{H}}_{BAB}(t)]_\parallel \\ \mathbf{0} & [\tilde{\mathbf{H}}_{ABA}(t)]_\parallel & [\tilde{\mathbf{H}}_{ABB}(t)]_\parallel & [\tilde{\mathbf{H}}_{ABAB}(t)]_\parallel \end{pmatrix}. \quad (46)$$

In the TD-EOM-CC method, truncated shifted Hamiltonian matrices generally exhibit this block structure. This is because the $\mathbf{U}(t)$ term given by Eq. (18) contributes to all upper triangular blocks of Eq. (46) except $\tilde{H}_{00}(t)$, the $\tilde{\mathbf{D}}(t)$ term given by Eq. (27) contributes to all diagonal blocks of the matrix, and the $\tilde{\mathbf{L}}(t)$ term given by Eq. (28) contributes to all lower triangular blocks of the matrix except $\tilde{H}_{00}(t)$.

If no further assumptions can be made regarding the block structure of $\tilde{\mathbf{H}}_\parallel(t)$ in Eq. (46), we cannot assume the correctness of the scaling properties of the method. This becomes apparent when considering that the block matrices in both Eqs. (41) and (46) can map partitions of right and transposed left amplitude vectors to partitions where the numbers of excited subsystems have both increased and decreased by one. Consequently, the products of two or more such matrices participating in $\mathbf{U}_\parallel(t_0, t)\mathbf{O}_\parallel(t)\mathbf{U}_\parallel(t, t_0)$ in Eq. (45) can result in a mapping between the nonzero 0 partition of $\mathbf{r}_\parallel(t_0)$ and the truncated AB partition of $\mathbf{l}_\parallel^T(t_0)$. This implies that time-dependent expectation values for two noninteracting subsystems, given by Eq. (42), are generally affected by the truncation of the product bases, that is,

$$\langle O(t)\rangle_\parallel \neq \mathbf{l}^T(t)\mathbf{O}(t)\mathbf{r}(t). \quad (47)$$

Thus, the scaling properties of the truncated TD-EOM-CC method are generally incorrect.

In the TDCC method, the $\tilde{\mathbf{L}}(t)$ term of the shifted Hamiltonian matrix $\tilde{\mathbf{H}}(t)$ is always zero, as seen from Eq. (30). In the TD-EOM-CC method, the $\tilde{\mathbf{L}}(t)$ term is zero whenever the interaction term $V(t)$ is zero, as seen from Eq. (28). In both these cases, the blocks below the diagonal of $\tilde{\mathbf{H}}_\parallel(t)$ are equal to zero and Eq. (46) can be written as

$$\tilde{\mathbf{H}}_\parallel(t) = \begin{pmatrix} \tilde{\mathbf{H}}_{00}(t) & \tilde{\mathbf{H}}_{0A}(t) & \tilde{\mathbf{H}}_{0B}(t) & \mathbf{0} \\ \mathbf{0} & \tilde{\mathbf{H}}_{AA}(t) & \mathbf{0} & [\tilde{\mathbf{H}}_{AAB}(t)]_\parallel \\ \mathbf{0} & \mathbf{0} & \tilde{\mathbf{H}}_{BB}(t) & [\tilde{\mathbf{H}}_{BAB}(t)]_\parallel \\ \mathbf{0} & \mathbf{0} & \mathbf{0} & [\tilde{\mathbf{H}}_{ABAB}(t)]_\parallel \end{pmatrix}. \quad (48)$$

The element $\tilde{H}_{00}(t)$ can also be eliminated in both methods by letting the time-dependent phase evolve according to Eq. (32). In the following discussion, however, we let the element be nonzero in order to demonstrate that the time dependence of the global phase does not have any impact on the scaling properties of the truncated methods.

We now examine how the vectors of the initial state are affected by the repeated transformation by shifted Hamiltonian

matrices with the block structure of Eq. (48). These matrices do not map partitions of right amplitude vectors to partitions with a higher number of excited subsystems. Consequently, assuming $\mathbf{r}(t_0) = \mathbf{r}_0^{(0)} = (1, \mathbf{0}, \mathbf{0}, \mathbf{0})^T$,

$$\tilde{\mathbf{H}}_\parallel(t_1) \cdots \tilde{\mathbf{H}}_\parallel(t_n) \mathbf{r}_\parallel(t_0) = \begin{pmatrix} [\tilde{\mathbf{H}}(t_1) \cdots \tilde{\mathbf{H}}(t_n)\mathbf{r}(t_0)]_0 \\ \mathbf{0} \\ \mathbf{0} \\ \mathbf{0} \end{pmatrix}, \quad (49)$$

where the right-hand side is described purely in terms of untruncated matrices and vectors, which is valid since the *AB* partition does not contribute to any of the matrix-vector transformations. Furthermore, the same matrices do not map partitions of transposed left amplitude vectors to partitions with a lower number of excited subsystems. Consequently,

$$\mathbf{l}_\parallel^T(t_0)\tilde{\mathbf{H}}_\parallel(t_n) \cdots \tilde{\mathbf{H}}_\parallel(t_1) = \begin{pmatrix} [\mathbf{l}^T(t_0)\tilde{\mathbf{H}}(t_n) \cdots \tilde{\mathbf{H}}(t_1)]_0 \\ [\mathbf{l}^T(t_0)\tilde{\mathbf{H}}(t_n) \cdots \tilde{\mathbf{H}}(t_1)]_A \\ [\mathbf{l}^T(t_0)\tilde{\mathbf{H}}(t_n) \cdots \tilde{\mathbf{H}}(t_1)]_B \\ [\mathbf{l}_\parallel^T(t_0)\tilde{\mathbf{H}}_\parallel(t_n) \cdots \tilde{\mathbf{H}}_\parallel(t_1)]_{AB} \end{pmatrix}^T, \quad (50)$$

where the 0, *A*, and *B* partitions on the right-hand side are described purely in terms of untruncated matrices and vectors, which is valid since the *AB* partition does not contribute to any of the corresponding matrix-vector transformations. Under the conditions that the matrix $\tilde{\mathbf{H}}(t)$ has the block upper triangular structure of Eq. (48) for all times t and that the right amplitude vector starts out as the ground-state vector $\mathbf{r}(t_0) = \mathbf{r}_0^{(0)}$, Eqs. (49) and (50) imply that

$$\mathbf{r}_\parallel(t) = \begin{pmatrix} [\mathbf{U}(t, t_0)\mathbf{r}(t_0)]_0 \\ \mathbf{0} \\ \mathbf{0} \\ \mathbf{0} \end{pmatrix}, \quad (51)$$

$$\mathbf{l}_\parallel^T(t) = \begin{pmatrix} [\mathbf{l}^T(t_0)\mathbf{U}(t_0, t)]_0 \\ [\mathbf{l}^T(t_0)\mathbf{U}(t_0, t)]_A \\ [\mathbf{l}^T(t_0)\mathbf{U}(t_0, t)]_B \\ [\mathbf{l}_\parallel^T(t_0)\mathbf{U}_\parallel(t_0, t)]_{AB} \end{pmatrix}^T, \quad (52)$$

where $\mathbf{U}(t, t_0)$ is the untruncated counterpart of the time evolution operator in Eq. (44), containing the untruncated time-dependent Hamiltonian matrices $\tilde{\mathbf{H}}(t)$ evaluated at different times t.

To assess the effect of truncation on time-dependent expectation values in the TDCC and field-free TD-EOM-CC methods, we note that the matrix $\mathbf{O}_\parallel(t)$ does not map between the 0 partition of right amplitude vectors and the *AB* partition of transposed left amplitude vectors. Hence, time-dependent expectation values for systems with two noninteracting subsystems, given by Eq. (45), are unaffected by the truncation of the product bases,

$$\langle O(t) \rangle_\parallel = \mathbf{l}_\parallel^T(t_0)\mathbf{U}_\parallel(t_0, t)\mathbf{O}_\parallel(t)\mathbf{U}_\parallel(t, t_0)\mathbf{r}_\parallel(t_0)$$

$$= [\mathbf{l}^T(t_0)\mathbf{U}(t_0, t)]_0 O_{00}(t)[\mathbf{U}(t, t_0)\mathbf{r}(t_0)]_0$$

$$+ [\mathbf{l}^T(t_0)\mathbf{U}(t_0, t)]_A \mathbf{O}_{A0}(t)[\mathbf{U}(t, t_0)\mathbf{r}(t_0)]_0$$

$$+ [\mathbf{l}^T(t_0)\mathbf{U}(t_0, t)]_B \mathbf{O}_{B0}(t)[\mathbf{U}(t, t_0)\mathbf{r}(t_0)]_0$$

$$= \mathbf{l}^T(t)\mathbf{O}(t)\mathbf{r}(t). \quad (53)$$

Furthermore, time-dependent expectation values can be shown to be unaffected by the truncation of the product bases for any number of noninteracting subsystems, by sequentially dividing one of the remaining composite subsystems into two subsystems and reapplying the aforementioned arguments. This implies that truncated TDCC and truncated field-free TD-EOM-CC methods have the correct scaling properties when the system starts out in the ground state.

III. COMPUTATIONAL DETAILS

In order to investigate the properties of the methods described in Sec. II B numerically, we truncate the methods at the CCSD level, giving the TD-EOM-CCSD and TDCCSD methods. The TD-EOM-CCSD method is implemented in the spin-adapted elementary basis in a development version of the e^T program [27], employing the time derivative of the global phase given by Eq. (32), which leads to $\tilde{D}_{\kappa\lambda}(t) = 0$ in Eq. (25). Furthermore, we use the existing implementations of the spin-adapted ground-state and TDCCSD methods in e^T (version 1.0) [27,28], which also employs Eq. (32). The methods are used to calculate the interaction of atoms with the electromagnetic field represented by the electric field

$$\boldsymbol{\mathcal{E}}(t) = \mathcal{E}_0 \cos[\omega_0(t - t_0) + \phi]f(t)\hat{\mathbf{e}}, \quad (54)$$

where $\mathcal{E}_0$ is the peak field strength, ω_0 the carrier frequency, ϕ the carrier-envelope phase, $f(t)$ the envelope, and $\hat{\mathbf{e}}$ the unit vector in the linear polarization direction of the field. The envelope is given the functional form

$$f(t) = \begin{cases} 0, & t < a \\ \sin^2\left(\frac{2\pi(t-a)}{4(b-a)}\right), & a \leqslant t \leqslant b \\ 1, & t > b, \end{cases} \quad (55)$$

which increases from zero to one in the interval from a to b.

The aug-cc-pVDZ basis set is used for the helium and beryllium atoms in the simulations. The field is given a carrier frequency of $1.005\,749\,62$ a.u., which corresponds to the transition between the ground $0\,^1S_0$ state and the first dipole-allowed excited $2\,^1P_1$ state of helium calculated with the EOM-CCSD method and the aug-cc-pVDZ basis set. By adopting this carrier frequency, the field is in resonance with the same transition for a single helium atom in both the TD-EOM-CCSD and TDCCSD simulations. The field is furthermore given a peak field strength of 3×10^{-2} a.u., a polarization in the z direction, and a carrier-envelope phase of $\phi = -\pi/2$. The envelope of the field is set to increase from $a = 0$ until $b = 15$ optical cycles (approximately 93.709 a.u.). The envelope gives the field a narrow bandwidth, centered around the $0\,^1S_0 - 2\,^1P_1$ resonance, which ensures that the time-dependent state of single-helium simulations is kept in a superposition dominated by the two states.

The integration of the time-dependent differential equations is performed with the Dormand-Prince 8(5, 3) method [29]. This method is an embedded explicit Runge-Kutta method that incorporates a primary solution accurate to the eighth order in the time-step size. Moreover, the method gives
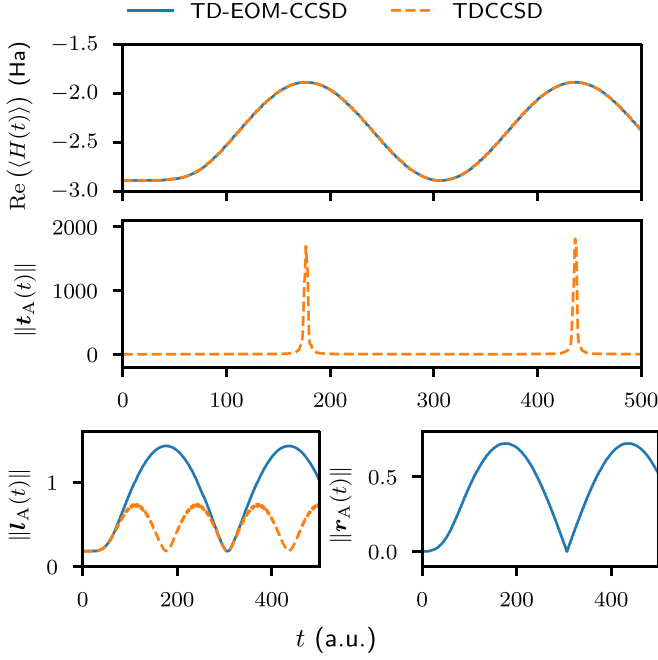
FIG. 1. Real part of the time-dependent energy expectation value Re[$\langle H(t) \rangle$] and 2-norms of the A partitions of the cluster, right, and left amplitudes $\|t_A(t)\|$, $\|r_A(t)\|$, and $\|l_A(t)\|$, respectively, from TD-EOM-CCSD and TDCCSD simulations of a single helium atom in an external field.

an estimate of the local integration error by using a combination of solutions with eighth-, fifth-, and third-order accuracy. The error estimate is used to adapt the time steps according to the procedure described in Appendix B of Ref. [24]. The initial time step size is set to 1×10^{-2} a.u. and the maximum and minimum values of the error estimate are set to 1×10^{-9} and 1×10^{-13} a.u., respectively. The integration is stopped when the size of the adaptive time step is smaller than 1×10^{-10}.

IV. RESULTS AND DISCUSSION

A. Simulating single-subsystem Rabi oscillations with the TD-EOM-CCSD and TDCCSD methods

For a single helium atom, both the TD-EOM-CCSD and TDCCSD methods can describe all possible excitations of the reference determinant, and the time-dependent observables are thus analytically equal for the two methods. In the top panel of Fig. 1, we show that this is also the case numerically for the real part of the time-dependent energy expectation value, as the two methods give indistinguishable results. The value is initially equal to the ground-state energy and periodically increases and decreases as a function of time, illustrating that the system undergoes Rabi oscillation between the $0\,^1S_0$ and $2\,^1P_1$ states of the helium atom. The maximum absolute value of the imaginary part of the expectation value is approximately $6 \times 10^{-14} E_h$ for the TD-EOM-CCSD method and $4 \times 10^{-12} E_h$ for the TDCCSD method, indicating that any unphysical imaginary energy components arising from the non-Hermitian nature of these methods can be disregarded in these cases. The time-dependent 2-norms of the A partitions of the cluster, right, and left amplitudes are also shown

in Fig. 1. In contrast to the right and left amplitude norms of both methods, the norm of the cluster amplitudes in the TDCCSD simulations displays narrow peaks which coincide with the maxima of the time-dependent energy expectation value. The TDCCSD method is known to be numerically unstable when the weight of the reference determinant approaches zero [20,21], but we observe that the method can still be used for simulating Rabi oscillations between the $0\,^1S_0$ and $2\,^1P_1$ states of a single helium atom.

B. Simulating two-subsystem Rabi oscillations with the TD-EOM-CCSD method

To numerically investigate the scaling properties of the TD-EOM-CCSD method, we simulate the interaction between two helium atoms and the external field, where one of the atoms is located at the origin and the other at $1 \times 10^7 a_0$ along the x axis. The large interatomic separation is chosen in order to minimize any interaction between the atoms, without requiring any modifications to the integral code. At this separation, the only nonzero two-center two-electron repulsion integrals (ERIs) are the ones of Coulomb type,

$$g_{\mu_A \nu_A \rho_B \sigma_B} = \int d\mathbf{r}_1 \int d\mathbf{r}_2 \frac{\rho_{\mu_A \nu_A}(\mathbf{r}_1) \rho_{\rho_B \sigma_B}(\mathbf{r}_2)}{|\mathbf{r}_1 - \mathbf{r}_2|}, \quad (56)$$

which asymptotically decay as the inverse distance between the electrons on the two centers due to the independence of the one-center orbital-pair densities $\rho_{\mu_A \nu_A}(\mathbf{r}_1) = \chi_{\mu_A}(\mathbf{r}_1)\chi_{\nu_A}(\mathbf{r}_1)$ and $\rho_{\rho_B \sigma_B}(\mathbf{r}_2) = \chi_{\rho_B}(\mathbf{r}_2)\chi_{\sigma_B}(\mathbf{r}_2)$ on the interatomic separation. The other two-center ERIs of exchange type,

$$g_{\mu_A \sigma_B \rho_B \nu_A} = \int d\mathbf{r}_1 \int d\mathbf{r}_2 \frac{\rho_{\mu_A \sigma_B}(\mathbf{r}_1) \rho_{\rho_B \nu_A}(\mathbf{r}_2)}{|\mathbf{r}_1 - \mathbf{r}_2|}, \quad (57)$$

are smaller than the default integral cutoffs of e^T and thus eliminated, due to their dependence on the two-center orbital-pair densities $\rho_{\mu_A \sigma_B}(\mathbf{r}_1) = \chi_{\mu_A}(\mathbf{r}_1)\chi_{\sigma_B}(\mathbf{r}_1)$ and $\rho_{\rho_B \nu_A} = \chi_{\rho_B}(\mathbf{r}_2)\chi_{\nu_A}(\mathbf{r}_2)$ which decay rapidly with increasing interatomic separation [30]. The two-center ERIs of Coulomb type have magnitudes of less than $1 \times 10^{-6} E_h$ in the simulations, implying that $H(t) \approx H_A(t) \otimes I_B + I_A \otimes H_B(t)$.

The simulation is successfully completed and the real part of the time-dependent energy expectation value and 2-norms of various amplitude partitions are shown together with the single-helium results of Sec. IV A in Fig. 2. The single-helium energy expectation value has been multiplied by a factor of two, since the correct scaling properties would require the two-helium energy expectation value to be equal to two times the single-helium one. The frequency of the oscillations in the scaled energy expectation value and single-subsystem norms increases, and their magnitude decreases, as the number of helium atoms increases from one to two. The maximum absolute value of the imaginary part of the energy expectation value is still small, at approximately $2 \times 10^{-6} E_h$.

A separate TD-EOM-CCSD simulation is performed where the two-center ERIs are eliminated. The results are shown in Fig. 2, demonstrating that the elimination of the integrals does not have any significant impact on the results. It further demonstrates that the incorrect scaling properties of the TD-EOM-CCSD method is not due to the weak interaction
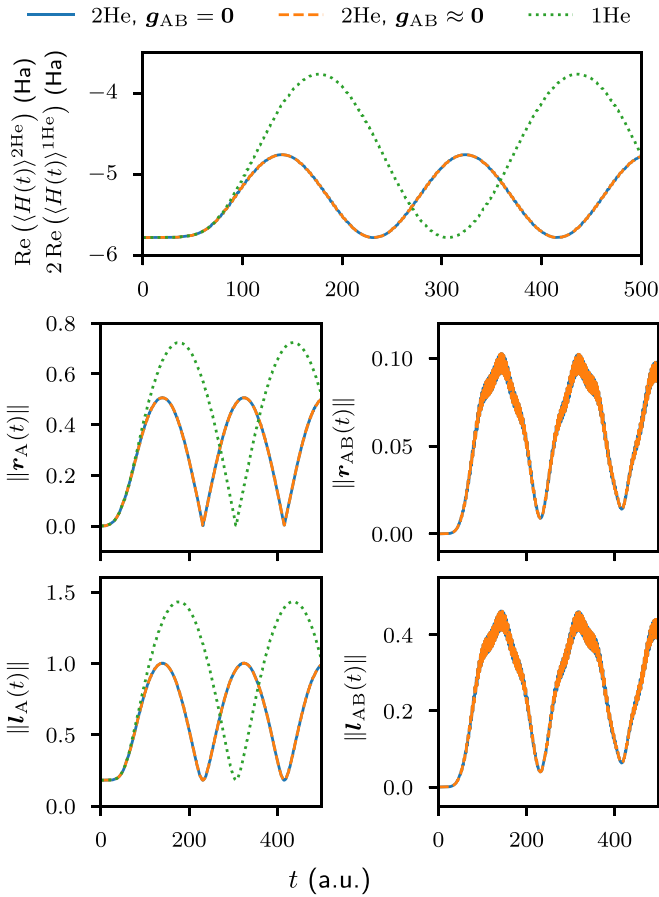
FIG. 2. TD-EOM-CCSD simulations of one (1He) and two distant (2He) helium atoms in an external field. Results from two different two-helium simulations are shown, one performed with the regular TD-EOM-CCSD method ($g_{AB} \approx 0$) and one where the two-center ERIs have been set to zero ($g_{AB} = 0$). The single-helium results in Fig. 1 are shown for comparison. In the top panel, the real part of the time-dependent energy expectation value $\mathrm{Re}[\langle H(t) \rangle]$ is shown, where the single-helium result has been multiplied a factor of two to better assess the scaling properties of the method. In the left column below the top panel, the 2-norms of the A partitions of the right and left amplitudes $\|r_A(t)\|$ and $\|l_A(t)\|$, respectively, are shown. In the right column, the 2-norms of the AB partitions of the right and left amplitudes $\|r_{AB}(t)\|$ and $\|l_{AB}(t)\|$, respectively, are shown.

between the distant electrons but rather a problem caused the insufficient flexibility of the parametrization of the method.

C. Simulating two-subsystem Rabi oscillations with the TDCCSD method

To numerically investigate the scaling properties of the TDCCSD method, we start by comparing the results from the single-helium simulation in Sec. IV A with results from simulations of two helium atoms, where one of the atoms is located at the origin and the other at $1 \times 10^7 a_0$ along the x axis. The large interatomic separation implies that Eq. (39) is approximately satisfied at the start of the simulation.

In Fig. 3 the real part of the time-dependent energy expectation value and 2-norms of various amplitude partitions are shown, for different two-helium TDCCSD simulations, and

compared to the results from the single-helium calculation in Sec. IV A. From the start of the simulation and up to 170 a.u. of time, the regular TDCCSD method gives an energy expectation value that is equal to two times the expectation value from the single-helium simulation, since the absolute difference between these quantities is on the order of 1×10^{-14} and less. This agrees with the theory in Sec. II C and implies that the TDCCSD method essentially treats the correlation exactly in this time interval, even though the system has four electrons and the operators in Eqs. (2) and (3) are truncated at the doubles level. The two-helium single-subsystem norms are also essentially equal to the single-helium norms in the same interval, as illustrated by the small absolute differences between these quantities. After around 170 a.u. of time, however, the regular TDCCSD simulation fails, and the integration stops as adaptive time steps smaller than 1×10^{-10} are needed to proceed. Toward the end of the simulation, the absolute differences between the two-helium and scaled single-helium results blow up by increasing several orders of magnitude, implying that the simulation does not behave according to the description in Sec. II C. Moreover, the norms of the AB partitions of both the cluster and left amplitudes rise throughout the simulation and also increase dramatically at the end. In the following, we argue that the blowup of the AB partitions of the amplitudes is the reason for the failure of the regular TDCCSD simulation.

The observed increase in the norm of the AB partition of the cluster amplitudes indicates that the conditions for Eq. (39) are not met exactly. To enforce this equation, a separate TD-CCSD simulation is conducted where the two-center ERIs are eliminated, which indeed results in the norm for the AB partition of the cluster amplitudes being equal to zero for all times t. However, the simulation still fails after around 170 a.u., and the 2-norm of the AB partition of the left amplitudes AB increases dramatically toward the end of the simulation, as shown in Fig. 3. The real part of the energy expectation value and single-subsystem 2-norms are also shown and compared to the scaled single-helium results in the figure. In contrast to the regular TDCCSD simulation, there are no visible instabilities in the absolute differences between the two-helium and scaled single-helium results, although the absolute difference in the energy expectation value has increased to a constant on the order of $1 \times 10^{-6} E_h$. This difference is larger than the one seen in the initial stages of the regular TDCCSD simulation and can be explained by the disruption of the equilibrium between the two-center electronic repulsion and nuclear attraction caused by the omission of the two-center ERIs. The difference can be expected to be smaller if all two-center interactions are removed from the integral code. Overall, the results support the correctness of the scaling properties of the TDCC method in the limit of no subsystem interaction but also highlight the sensitivity of the cluster amplitudes to interactions between the two subsystems in simulations of collective Rabi oscillations.

Provided the AB partition of the cluster amplitudes is zero in the TDCC method, Eq. (53) predicts that time-dependent expectation values should not depend on the AB partition of the left amplitudes. To verify this prediction and evaluate the impact of eliminating the AB partition of both vectors on the numerical stability, a separate simulation is conducted where the two-center ERIs and the initial values and time derivatives
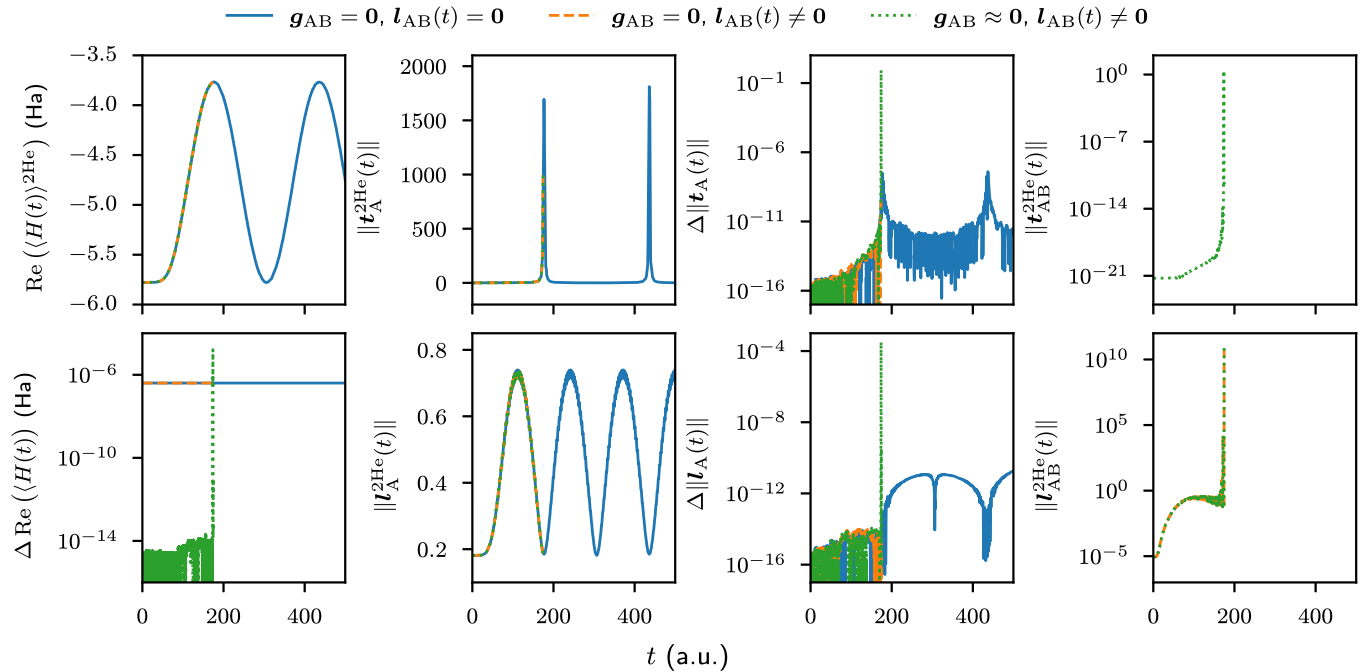
FIG. 3. TDCCSD simulations of one (1He) and two distant (2He) helium atoms in an external field. Results from three different two-helium simulations are shown, one performed with the regular TDCCSD method [$g_{AB} \approx 0$ and $l_{AB}(t) \neq 0$], one where the two-center ERIs have been set to zero [$g_{AB} = 0$ and $l_{AB}(t) \neq 0$], and one where both the two-center ERIs and the AB partition of the left amplitudes have been set to zero [$g_{AB} = 0$ and $l_{AB}(t) = 0$]. The first column of panels shows the real part of the time-dependent energy expectation value $\mathrm{Re}[\langle H(t) \rangle^{2\mathrm{He}}]$ and the absolute difference $\Delta \mathrm{Re}[\langle H(t) \rangle] = |\mathrm{Re}[\langle H(t) \rangle^{2\mathrm{He}}] - 2\mathrm{Re}[\langle H(t) \rangle^{1\mathrm{He}}]|$ with the single-helium result multiplied by a factor of two. In the second column, the 2-norms of the A partitions of the cluster and left amplitudes $\|t_A^{2\mathrm{He}}(t)\|$ and $\|l_A^{2\mathrm{He}}(t)\|$ are shown. In the third column the absolute differences $\Delta\|t_A(t)\| = |\|t_A^{2\mathrm{He}}(t)\| - \|t_A^{1\mathrm{He}}(t)\||$ and $\Delta\|l_A(t)\| = |\|l_A^{2\mathrm{He}}(t)\| - \|l_A^{1\mathrm{He}}(t)\||$ with the single-helium norms are shown. In the last column, the 2-norms of the AB partitions of the cluster and left amplitudes $\|t_{AB}^{2\mathrm{He}}(t)\|$ and $\|l_{AB}^{2\mathrm{He}}(t)\|$, respectively, are shown.

of the AB partition of the left amplitudes are set to zero. This simulation is successfully completed, demonstrating that the failure of the previous simulation is caused by the AB partition of the left amplitudes. In Fig. 3 the resulting real part of the energy expectation value and 2-norms of single-subsystem amplitude partitions are shown and compared to the scaled single-helium results. The absolute differences between the two-helium and scaled single-helium results are consistently below 1×10^{-6} and there is no visible difference in the energy expectation value caused by the removal of the AB partition of the left amplitudes, in agreement with the theoretical observations made in Sec. II C. Furthermore, the maximum absolute value of the imaginary part of the energy expectation value is negligible, at approximately $4 \times 10^{-12} E_\mathrm{h}$.

D. Scaling of collective Rabi oscillations with the number of subsystems

To further investigate the scaling properties of the TD-EOM-CCSD and TDCCSD methods, the interaction with the field is also calculated for three to five helium atoms and for one helium atom together with one to two beryllium atoms. The first helium atom is located at the origin and the following atoms at increments of $1 \times 10^7 a_0$ along the x axis. In all simulations, the two-center ERIs are eliminated to avoid the blowup of the AB partition of the cluster amplitudes in the TDCCSD simulation and to treat the two methods on an equal footing. Furthermore, the initial values and time derivatives of

the AB partition of the left amplitudes are also set to zero in all TDCCSD simulations. All simulations complete successfully, and for both methods the maximum absolute value of the imaginary parts of the energy expectation value comes from the simulations with one helium and two beryllium atoms, at approximately $3 \times 10^{-5} E_\mathrm{h}$ for the TD-EOM-CCSD method and $2 \times 10^{-8} E_\mathrm{h}$ for the TDCCSD method.

To estimate the Rabi frequencies Ω from the simulation results, the sinusoidal function $A \sin(\Omega t + \varphi) + C$ is least-squares fitted to the real part of the oscillating time-dependent energy expectation value between $t = 100$ and 500 a.u. The resulting frequencies are displayed in Fig. 4. From the figure we can see that the Rabi frequencies from the TD-EOM-CCSD simulations increase with the number of helium atoms. The function $A\sqrt{n_\mathrm{He}} + C$ is least-squares fitted to these frequencies to evaluate their scaling properties, where n_He represents the number of helium atoms. The fitted curve, also illustrated in Fig. 4, demonstrates that the Rabi frequency increases as the square root of the total number of helium atoms. As the number of subsystems in resonance with the field increases, the frequency can therefore erroneously appear to approach infinity, meaning the TD-EOM-CCSD method gives a qualitatively incorrect representation of transitions occurring in multiple subsystems simultaneously. This scaling behavior is similar to the physical square-root scaling that can be observed when a single excitation is symmetrically shared among N atoms experiencing effectively uniform coupling and interaction, such as when multiatom Rydberg
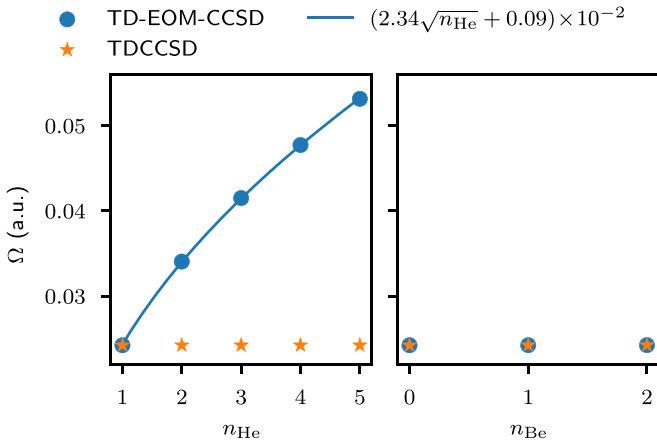
FIG. 4. TD-EOM-CCSD and TDCCSD simulations of distant helium and beryllium atoms in an external field, with the two-center ERIs and the *AB* partition of the TDCC left amplitudes set to zero. The left panel shows results for one to five helium atoms and the right panel results for one helium atom and zero to two beryllium atoms. The Rabi frequencies Ω are obtained by least-squares fitting the function $A\sin(\Omega t + \varphi) + C$ to the real part of the time-dependent energy expectation value. The function $(2.34\sqrt{n_{\mathrm{He}}} + 0.09) \times 10^{-2}$ is obtained by least-squares fitting the function $A\sqrt{n_{\mathrm{He}}} + C$ to the TD-EOM-CCSD Rabi frequencies shown in the left panel.

excitations are blocked by van der Waals interactions [31]. In our simulations, however, the scaling effect is caused by the limited flexibility of the TD-EOM-CCSD parametrization, as removing the two-center ERIs has no discernible impact on the results in Sec. IV B.

For all TDCCSD simulations, the Rabi frequencies shown in Fig. 4 remain constant regardless of the number of helium or beryllium atoms, as predicted in Sec. II C. In addition, the Rabi frequencies also remain constant in TD-EOM-CCSD simulations involving a helium atom and up to two beryllium atoms, suggesting that Rabi frequencies in the TD-EOM-CC simulation are insensitive to the number of off-resonant subsystems. Therefore, TD-EOM-CC simulations may provide an accurate portrayal of a solitary Rabi oscillation in an extended quantum system while maintaining superior numerical stability compared to TDCCSD simulations.

V. CONCLUSION

In this work a general theoretical framework for representing both the TD-EOM-CC and TDCC methods was presented, incorporating the time derivatives of the cluster amplitudes as auxiliary conditions. Through this framework, it was demonstrated that the scaling properties of truncated TD-EOM-CC methods are incorrect in general, while the scaling properties are correct for truncated TDCC and field-free TD-EOM-CC methods.

The TD-EOM-CCSD method was implemented in the elementary basis and used to numerically compare the scaling properties of the TD-EOM-CCSD and TDCCSD methods through simulations of collective Rabi oscillations. The simulations revealed that the TD-EOM-CCSD method gives a qualitatively incorrect representation of collective Rabi oscillations, since the Rabi frequency increases with the number of subsystems in resonance with the external field. Nevertheless, the results also indicate that truncated TD-EOM-CC methods can be suitable for simulating solitary Rabi oscillations in extended quantum systems.

All TD-EOM-CCSD simulations were successfully completed, while the regular TDCC simulations of collective Rabi oscillations in distant subsystems failed due to the cluster and left amplitudes blowing up. Despite this, the initial stages of the TDCCSD simulations displayed the correct scaling properties, as predicted by Sec. II C, suggesting that the TDCC method can be suitable for simulating collective transitions in extended systems, as long as complete population inversion is avoided. Furthermore, it was demonstrated that the numerical stability of the TDCC simulations can be enhanced by ensuring that all two-center ERIs are precisely zero and eliminating the two-subsystem deexcited partition of the left amplitudes. However, this approach is not suitable when simulating collective Rabi oscillations in systems that necessitate the description of interaction between subsystems.

In conclusion, we propose that further research should be dedicated to the development of approximate methods that can provide a qualitatively correct description of collective Rabi oscillations, even when the interaction between the subsystems is nonzero.

[1] T. Brabec and F. Krausz, Rev. Mod. Phys. **72**, 545 (2000).

[2] E. A. Seddon, J. A. Clarke, D. J. Dunning, C. Masciovecchio, C. J. Milne, F. Parmigiani, D. Rugg, J. C. H. Spence, N. R. Thompson, K. Ueda, S. M. Vinko, J. S. Wark, and W. Wurth, Rep. Prog. Phys. **80**, 115901 (2017).

[3] J. Duris, S. Li, T. Driver, E. G. Champenois, J. P. MacArthur, A. A. Lutman, Z. Zhang, P. Rosenberger, J. W. Aldrich, R. Coffee, G. Coslovich, F.-J. Decker, J. M. Glownia, G. Hartmann, W. Helml, A. Kamalov, J. Knurr, J. Krzywinski, M.-F. Lin, J. P. Marangos *et al.*, Nat. Photon. **14**, 30 (2020).

[4] V. Stooß, S. M. Cavaletto, S. Donsa, A. Blättermann, P. Birk, C. H. Keitel, I. Březinová, J. Burgdörfer, C. Ott, and T. Pfeifer, Phys. Rev. Lett. **121**, 173005 (2018).

[5] Y. Silberberg, Annu. Rev. Phys. Chem. **60**, 277 (2009).

[6] K. Kulander and M. Lewenstein, in *Springer Handbook of Atomic, Molecular, and Optical Physics*, edited by G. Drake (Springer, New York, 2006), pp. 1077–1089

[7] T. Bayer, M. Wollenhaupt, and T. Baumert, J. Phys. B **41**, 074007 (2008).

[8] A. Hishikawa, A. Matsuda, and M. Fushitani, Bull. Chem. Soc. Jpn. **93**, 1293 (2020).

[9] I. R. Solá, J. González-Vázquez, R. de Nalda, and L. Bañares, Phys. Chem. Chem. Phys. **17**, 13183 (2015).

[10] A. Palacios and F. Martín, WIREs Comput. Mol. Sci. **10**, e1430 (2020).

[11] H. R. Larsson, S. Bauch, L. K. Sørensen, and M. Bonitz, Phys. Rev. A **93**, 013426 (2016).

[12] M. Labeye, F. Zapata, E. Coccia, V. Véniard, J. Toulouse, J. Caillat, R. Taïeb, and E. Luppi, J. Chem. Theory Comput. **14**, 5846 (2018).

[13] X. Li, N. Govind, C. Isborn, A. E. DePrince III, and K. Lopata, Chem. Rev. **120**, 9951 (2020).

[14] R. J. Bartlett, in *Theory and Applications of Computational Chemistry*, edited by C. E. Dykstra, G. Frenking, K. S. Kim, and G. E. Scuseria (Elsevier, Amsterdam, 2005), pp. 1191–1221.

[15] F. A. Evangelista, J. Chem. Phys. **149**, 030901 (2018).

[16] R. J. Bartlett, Annu. Rev. Phys. Chem. **32**, 359 (1981).

[17] H. Koch, H. J. A. Jensen, P. Jørgensen, and T. Helgaker, J. Chem. Phys. **93**, 3345 (1990).

[18] H. Koch, R. Kobayashi, A. Sanchez de Merás, and P. Jørgensen, J. Chem. Phys. **100**, 4393 (1994).

[19] M. Nooijen, K. R. Shamasundar, and D. Mukherjee, Mol. Phys. **103**, 2277 (2005).

[20] T. B. Pedersen and S. Kvaal, J. Chem. Phys. **150**, 144106 (2019).

[21] H. E. Kristiansen, Ø. S. Schøyen, S. Kvaal, and T. B. Pedersen, J. Chem. Phys. **152**, 071102 (2020).

[22] J. A. Sonk, M. Caricato, and H. B. Schlegel, J. Phys. Chem. A **115**, 4678 (2011).

[23] E. Luppi and M. Head-Gordon, Mol. Phys. **110**, 909 (2012).

[24] A. S. Skeidsvoll, T. Moitra, A. Balbi, A. C. Paul, S. Coriani, and H. Koch, Phys. Rev. A **105**, 023103 (2022).

[25] H. Koch and P. Jørgensen, J. Chem. Phys. **93**, 3333 (1990).

[26] T. B. Pedersen, H. E. Kristiansen, T. Bodenstein, S. Kvaal, and Ø. S. Schøyen, J. Chem. Theory Comput. **17**, 388 (2021).

[27] S. D. Folkestad, E. F. Kjønstad, R. H. Myhre, J. H. Andersen, A. Balbi, S. Coriani, T. Giovannini, L. Goletto, T. S. Haugland, A. Hutcheson, I.-M. Høyvik, T. Moitra, A. C. Paul, M. Scavino, A. S. Skeidsvoll, Å. H. Tveten, and H. Koch, J. Chem. Phys. **152**, 184103 (2020).

[28] A. S. Skeidsvoll, A. Balbi, and H. Koch, Phys. Rev. A **102**, 023115 (2020).

[29] E. Hairer, G. Wanner, and S. P. Nørsett, *Solving Ordinary Differential Equations I: Nonstiff Problems*, Springer Series in Computational Mathematics Vol. 8 (Springer, Berlin, 1993), pp. 129–353.

[30] T. Helgaker, P. Jørgensen, and J. Olsen, *Molecular Electronic-Structure Theory* (Wiley, New York, 2000), Chap. 9, pp. 336–432.

[31] J. Zeiher, P. Schauß, S. Hild, T. Macrì, I. Bloch, and C. Gross, Phys. Rev. X **5**, 031015 (2015).